energies

MDPI

Article

Engineering of Hybrid SiO_2@{N-P-Fe} Catalysts with Double-Ligand for Efficient H_2 Production from HCOOH

Anna Sotiriou [1], Eleni Aspri [1], Yiannis Deligiannakis [2,*] and Maria Louloudi [1,*]

[1] Laboratory of Biomimetic Catalysis & Hybrid Materials, Department of Chemistry, University of Ioannina, 45110 Ioannina, Greece
[2] Laboratory of Physical Chemistry of Materials & Environment, Department of Physics, University of Ioannina, 45110 Ioannina, Greece
* Correspondence: ideligia@uoi.gr (Y.D.); mlouloud@uoi.gr (M.L.)

Abstract: Two Fe-based hybrids, [SiO_2@NP(Ph)$_2$/Fe^{II}/PP_3] and [SiO_2@NP(t-Bu)$_2$/Fe^{II}/PP_3], were synthesized using the double-ligand approach by covalently grafting NP ligands onto the surface of SiO_2. Both catalytic systems were evaluated for H_2 production through formic acid dehydrogenation (FADH), revealing important efficiency without requiring additional additives and/or co-catalysts. During the continuous addition of FA, [SiO_2@NP(Ph)$_2$/Fe^{II}/PP_3] and [SiO_2@NP(t-Bu)$_2$/Fe^{II}/PP_3] demonstrated great stability, achieving total TONs = 20,636 and 20,854, respectively. FT-IR and Raman spectroscopy provided insights into the role of NP ligands, such as NP(Ph)$_2$ and NP(t-Bu)$_2$, on the assembly and structural configuration of active hybrid Fe catalysts and their ability to dehydrogenate formic acid. Additional studies, including in situ mapping of the solution potential (E_h) of the catalytic reaction and an Arrhenius study of the activation energy (E_a), revealed a correlation between E_a and H_2 production rates: the system [SiO_2@NP(Ph)$_2$/Fe^{II}/PP_3] with an E_a = 29.4 KJ/mol shows an H_2 production rate of 58 mL-H_2/min, while [SiO_2@NP(t-Bu)$_2$/Fe^{II}/PP_3] with a E_a = 50.6 KJ/mol shows an H_2 production rate of 55 mL-H_2/min. This is the first example of a heterogeneous FADH system where the original strategy of a "double-ligand" has been demonstrated for homogeneous FADH catalytic systems. Herein we demonstrate that we can engineer a decrease in the activation barrier Ea via two synergistic steps: (i) via grafting of the NP ligand onto SiO_2 and (ii) using PP_3 as double ligand. This strategy leads to a boost in the H_2 production efficiency of [SiO_2@NP(Ph)$_2$/Fe^{II}/PP_3] as a heterogeneous catalyst, which for the first time has been shown to be able to outperform the parental reference/homogenous catalyst [Fe^{II}/PP_3].

Keywords: H_2 production; FADH; formic acid; Fe catalyst; NP ligands

check for updates

Academic Editor: Luca Gonsalvi

Received: 28 December 2024
Revised: 16 January 2025
Accepted: 21 January 2025
Published: 23 January 2025

Citation: Sotiriou, A.; Aspri, E.; Deligiannakis, Y.; Louloudi, M. Engineering of Hybrid SiO_2@{N-P-Fe} Catalysts with Double-Ligand for Efficient H_2 Production from HCOOH. *Energies* **2025**, *18*, 514. https://doi.org/10.3390/en18030514

Copyright: © 2025 by the authors. Licensee MDPI, Basel, Switzerland. This article is an open access article distributed under the terms and conditions of the Creative Commons Attribution (CC BY) license (https://creativecommons.org/licenses/by/4.0/).

1. Introduction

During recent years, with the necessary shift in energy policies towards more green/sustainable technologies, H_2 has been identified as a highly potent sustainable energy source, mainly due to its high energy density of *ca* 143 MJ kg^{-1} and as key component in H_2 fuel cells. However, as a fuel, hydrogen is not naturally available for immediate use. Apart from its production via H_2O electrolysis, it can be obtained via the dehydrogenation of liquid compounds known as Liquid Organic Hydrogen Carriers (LOHCs) such as formic acid (HCOOH) [1–5]. Formic acid can release H_2 under mild conditions, with a hydrogen content of 4.4% wt [6]. Its decomposition can occur through two pathways: (1) the formation of CO, which is toxic for fuel cells and therefore is a prohibited reaction

pathway and (2) the production of the desired H_2 gas along with CO_2 in a 1:1 ratio. Although Reaction (2) is thermodynamically favored ($\Delta G = -32.9$ KJ mol^{-1}), the presence of a catalyst is crucial to also guarantee a kinetic preference [7].

$$HCOOH \rightarrow CO(g) + H_2O(l)\ (\Delta G = -12.4\ \text{KJ mol}^{-1}) \quad (1)$$

$$HCOOH \rightarrow H_2(g) + CO_2(g)\ (\Delta G = -32.9\ \text{KJ mol}^{-1}) \quad (2)$$

The idea of dehydrogenation was initially examined using various noble metal centers such as Pt, Rh, and Pd. The first approach was developed in 1967 by Coffey, who developed catalysts with phosphine ligands and Ru- and Ir- metal centers that were used for formic acid dehydrogenation [8]. Over the years, many individuals developed significant catalytic systems, such as Gao and Puddephat [9], Laurenczy [10], and Himeda [11]. Meanwhile, Beller conducted studies on the systems $RhCl_3 \cdot xH_2O$ and $RuBr_3 \cdot xH_2O$ and the precursors $[RuCl_2(\text{p-cymene})]_2$, $[RuCl_2(\text{benzene})]_2$, and $[RCl_3(PPh_3)_3]_2$ in the presence of additives such amines like NEt_3. In his work, he also examined the influence of phosphine ligands on Ru-based catalysts [12,13].

In this context, it is becoming clear that the selection of the right ligand is crucial for creating an efficient catalyst. Ligands are coordinated to the metal center, determining some of its steric and electronic properties as well as the key interactions between the metal and substrate. Accordingly, most ligands used so far are based on atoms and active groups that are capable of acting as σ-donors or/and π-acceptors, e.g., P and N atoms, with P being a stronger donor than N [14]. PNP ligands fall into this category of ligands, which are specifically known as "pincer" ligands, since they can pinch the metal center, creating a well-established coordination environment with the substrate and leading to enhanced catalytic performance [13,14]. Thus, in recent studies Pan et al. [15] reported homogeneous Ru catalysts employing pyridine-based ligands that can undergo dearomatization via the deprotonation of the NH-P(^{t}Bu) arm. These catalysts exhibited excellent stability in the presence of water and oxygen, but the best catalytic results were obtained in a DMSO solvent, achieving TOFs of 7000 h^{-1} over a period of 9000 min. The rate of hydrogen production was increased by the addition of an external base, which affected the catalyst's lifetime. Nevertheless, the exceptional catalytic performance of noble-based metal centers tends to pose challenges, i.e., in terms of cost and resource limitations. Therefore, the scientific community has been focusing on developing catalysts based on non-noble transition metals, which are abundant and cost-effective. So far, most complexes investigated in this category are first-row transition metals, e.g., Fe-based, but lately more catalysts have been developed that incorporate Ni [16], Cu [17], and Al [18,19].

Within this context, Milstein et al. developed an Fe–PNP complex using an Fe-center ($Fe(BF_4)_2 \cdot 6H_2O$), as was originally conceptualized by Beller et al. in 2011 [20]. In [21], a $^{t\text{Bu}}$-PNP (2,6-bis(di-*tert*-butylphosphinomethyl)pyridine) was used to synthesize the active center ($^{t\text{Bu}}$PNP)Fe(H)$_2$(CO) for HCOOH dehydrogenation in a 1,4-dioxane solvent with the addition of NEt_3. This system achieved a rather low TOF = 416 h^{-1} [21] at T = 40 °C. The idea of using PNP ligands for FADH has been further explored in [22], resulting in an Fe- $^{i\text{Pr}}$PN$^{\text{Me}}$P ($CH_3N(CH_2CH_2P^iPr_2)_2$) that achieved a significantly high value for TONs (>100,000) under additive-free conditions in a toluene solvent [22]. As shown in [22], the catalyst's performance, compared to a corresponding $^{i\text{Pr}}$PN$^{\text{H}}$P complex, reached a TON = 1400 under the same conditions, which is due to its structural modification offering greater stability [22]. In 2019, Tondreau et al. presented a [(^{t}BuPNNOP)Mn(CO)$_2$]Br catalyst for hydrogen production in a chlorobenzene solvent along with the addition of NEt_3 at 80 °C. The Mn catalyst reached a TON = 20,000 and a TOF = 8500 h^{-1} [23].

A further key realm in catalytic H_2 production via FADH is heterogeneous catalytic systems, i.e., systems created by immobilizing ligands and/or metal complexes on the surface of appropriate solid matrices. The first example of this approach occurred in 2011, when Zhao et al. [24] developed Pd-S-SiO_2 and Ru-S-SiO_2 catalysts. These systems were used for FADH in a 4M aqueous HCOOH solution in the presence of HCOONa at 85 °C, reaching a TOF = 700 h^{-1} [24]. In 2015, we reported the development of two hybrid materials by immobilizing phosphine ligands on SiO_2, i.e., {RPh_2@SiO_2} and {polyRPhphos@SiO_2} [25]. The catalytic complexes of these hybrid materials demonstrated a very high FADH at P = 1 atm and T = 80 °C, exhibiting a total TONs of 176,000 and 65,000, respectively [25].

Later, we introduced the "double-ligand" approach in homogeneous systems [14]. In this approach, we proposed a combination of a phosphine-based PP_3 (L_1), $[(C_6H_5)PCH_2CH_2]_3P$, and a Schiff base (L_2) ligand, coupled to the same Fe^{II} center [14]. The corresponding Ru-based catalyst was also synthesized [14]. This study was the first to underline that a non-noble metal system (Fe) could outperform its noble counterpart (Ru) (PP_3RuL_2: TONs > 17,367 and PP_3FeL_2: TONs > 29,372). The catalytic process was conducted at 90 °C with the incorporation of the heterogeneous co-catalyst NH_2@SiO_2 [1]. Following this approach, Gkatziouras et al. demonstrated the advancement of Fe–imidazole nanohybrids using SiO_2 [26] and activated carbon [27] as support materials. The latter hybrid exhibited excellent reusability, achieving a TON > 428,000 in more than eight cycles [27]. Recently [28], we used the "double-ligand" approach to combine two PNP ligands: bis[(2-di-isopropylphosphino)ethyl]amine (^{iPro}PNP) and [2-(di-tertbutylphosphino)ethyl]amine (^{tBu}PNP).

Herein, aiming to address any limitations of the heterogenized catalytic systems, we introduce the development of new catalysts by covalently grafting two cost-effective NP ligands onto the surface of SiO_2. The obtained hybrids are synthesized in situ without the need for any additives, offering a new low-cost and easy-to-handle alternative for FADH catalysis. Through catalytic, spectroscopic, and thermodynamic studies, new insights are presented in order to provide more knowledge of the operation of both homogeneous and heterogeneous systems. Moreover, the anticorrelation between the activation energies and the simultaneous increase in the gas production rate is clarified and further discussed.

2. Materials and Methods

2.1. Materials

Propyl-carbonate (PC), $Fe(BF_4)_2 \cdot 6H_2O$, tris-2-(diphenylphosphino)ethyl phosphine (PP_3, $[(C_6H_5)PCH_2CH_2]_3P$, 97% purity), and 3-(diphenylphosphino)-1-propylamine ($NP(Ph)_2$, $C_{15}H_{18}NP$) were purchased from Sigma-Aldrich, 3050 Spruce Street, St. Louis, MO, USA, and kept under Ar. FA (Formic Acid, 97.5/2.5 H_2O *v*/*v*) was obtained from Supelco, 64271 Dermastadt, Germany, while 3-(Di-t-butylphosphino)propylamine ($NP(t\text{-}Bu)_2$, $C_{11}H_{26}NP$) was from Strem Chemicals, 7 Mulliken Way, Newburyport, MA, USA.

2.2. Characterization Techniques

Thermogravimetric analysis (TG-DTA): For the thermogravimetric analysis (TGA-DTA), a SETARAM (Caluire-et-Cuire, France) TGA 92 analyzer was utilized, with a heating rate of 5 °C/min, covering a range between 20 °C and 700 °C, and with an oxygen gas carrier flow rate of 20 mL/min.

Fourier transformed infrared spectroscopy (FT-IR): FT-IR spectra were acquired in the range of 4000 to 400 cm^{-1}, with a resolution of 4, and a total of 100 scans using a Nicolet IS5 system with OMNIC FTIR Software (9.2.86 version). The materials were dispersed in KBr pellets.

Raman spectroscopy: Raman spectroscopy evaluations were conducted on a Raman HORIBA-Xplora Plus spectrometer coupled with an Olympus (Tokyo, Japan) BX41 micro-

scope. A 785 nm diode laser served as the excitation source, while the laser beam focused onto the sample with the help of a microscope. Due to the powdery nature of the materials, a pellet was formed by pressing them gently between two glass plates. It is crucial to mention that the crystal phase of the materials was preserved by using a 15 mW laser.

In situ Monitoring of Solution Potential (E_h): As we have shown previously [26,28,29], solution potential E_h provides key insights into the reductive evolution of the FADH systems, which is related to the formation of the key intermediate product [Metal–Hydride] [29]. Herein, the solution potential Eh was monitored continuously in situ during the catalytic reactions, using a combined Pt-ring electrode (Hanna (Smithfield, RI, USA), HI36180) calibrated vs. Standard Hydrogen Electrode (SHE). The electrode was immersed directly into the catalytic reaction, in a wide-neck tube to assist with constant stirring and accessibility practices [26]. E_h measurements occurred with every reagent addition, according to the established catalytic procedure.

2.3. Synthesis of Hybrid Materials

For the preparation of the hybrid materials, 1 mmol of the NP ligands ($NP(Ph)_2$ and $NP(^tBu)_2$) and 1 mmol of 3-chloropropyl-trimethoxy-silane ($C_6H_{15}ClO_3Si$) were introduced to 15 mL of MeOH. The resulting solution was refluxed with stirring for 24 h at 60 °C. Then, 400 mg of dried colloidal SiO_2 and 5 mL of EtOH were added. The suspension was refluxed for an additional 24 h, resulting in the formation of the hybrid materials, which were then rinsed three times with methanol and then dried under vacuum for 24 h at 80 °C.

2.4. Catalytic HCOOH-Dehydrogenation Procedure

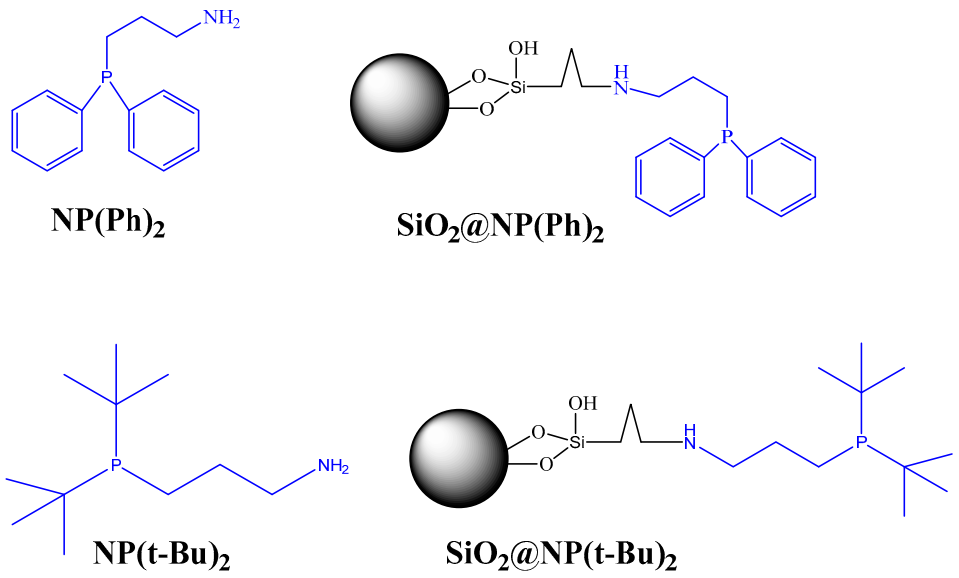
In a typical catalytic experiment, 7.5 μmol of $Fe(BF_4)_2 \cdot 6H_2O$ was dispersed in a 7 mL solution of PC/FA at a 5:2 (v/v) ratio each. Consequently, 15 μmol of each NP ligand was added. The resulting mixture was left under vigorous stirring for 15 min, after which 15 μmol of PP3 was introduced to the catalytic reaction. All catalytic experiments were conducted at a temperature of 80 °C, in a double-walled thermostatic reactor with constant stirring. The reactor was linked to a GC system (Shimadzu (Kyoto, Japan) GC-2014 Gas Chromatograph with a Thermal Conductive Detector (GC-TCD) that had been enhanced with a Carboxen-1000 column), while the released gases were measured using a manual gas burette. For the continuous operation catalytic experiments, 1 mL of FA was added to the reaction for every 1.2 L of gases produced.

Recycling experiments: To recover the catalytic materials, the reaction mixture was collected and centrifuged at 6000 rpm for 15 min. The obtained solid was washed three times with methanol and dried at 80 °C in dry pistol under vacuum. For the recycling tests, the same catalytic procedure was followed, except that the recovered catalyst was used instead of a new addition of NP hybrids and Fe^{II} salt. Calculation of TONs and TOFs were conducted using the equations mentioned in previous publications by our group [1,30] and are given in Supplementary Materials as Equations (S1) and (S2).

3. Results

3.1. Synthesis and Characterization of Hybrid Materials

Synthesis: The hybrid materials presented herein (Scheme 1) were prepared by a reaction of the NP organic compounds ($NP(Ph)_2$, $NP(t\text{-}Bu)_2$) via their terminal NH_2 group with 3-chloropropyl-trimethoxy-silane ($C_6H_{15}ClO_3Si$) with the corresponding n-propyl-$HNP(Ph)_2$- and n-propyl-$HNP(t\text{-}Bu)_2$-silane derivatives, which subsequently were covalently grafted on the SiO_2 surface via co-condensation.



Scheme 1. Structure of the NP-ligands and their immobilized counterparts.

TG-DTA analysis: The thermogravimetric analysis of the SiO_2@NP hybrids (see thermographs in Figures S1 and S2) provided insights into the loading of the ligands on the SiO_2 surface, as considered with respect to the observed mass loss, and accompanied by exothermic–endothermic curves. The major combustion attributed to the NP ligands developed between 220 and 520 °C. Based on the mass loss, the ligand loading for SiO_2@NP(Ph)$_2$ was calculated to be 12%, correlating with 0.33 mmol of NP(Ph)$_2$/g of material. For SiO_2@NP(t-Bu)$_2$, the ligand loading reached 7.4%, a percentage that is equal to 0.30 mmol of NP(t-Bu)$_2$/g.

FT-IR spectroscopy: For the FT-IR spectra of the SiO_2@NP(Ph)$_2$ and SiO_2@NP(t-Bu)$_2$ materials (Figure S3), the bands that appeared at 806–812, 465, and 1087–1100 cm^{-1} can be attributed to the stretching vibrations of the Si-O-Si and Si-O bonds, respectively. The band detected at 1625 cm^{-1} is associated with the bending vibrations of the Si-OH bond [31,32]. For the reader's convenience, the vibrations that refer to the SiO_2 matrix are marked with red dotted lines. The successful grafting of the NP ligands is supported by the appearance of some unique bands derived from the vibrations of the NP organic functionalities, i.e., the peaks between 2850 and 3000 cm^{-1} that correspond to the aliphatic and aromatic vibrations of the C-H bonds, those at 592 and 698 cm^{-1} that are associated with the stretching vibrations of the P-C bond for SiO_2@NP(Ph)$_2$ (Figure S3a) [28], and those at 581 cm^{-1} that refer to the P-C vibrations for SiO_2@NP(t-Bu)$_2$ (Figure S3b) [33].

Raman spectroscopy: The modified materials were further characterized using Raman spectroscopy (Figure S4). The SiO_2 matrix exhibits a specific band at ~800 cm^{-1}, corresponding to the symmetrical stretching vibrations of Si-O-Si [34]. Generally, the inter-tetrahedral modes of siloxane (Si-O-Si) from the silica support appear at 300–600 cm^{-1}, whilst the bending O-H vibrations from the Si-OH ends appear at around 900 cm^{-1} [35,36]. The organic NP ligands display several peaks that can be assigned to various vibrations, i.e., ν(P-C) (594–709 cm^{-1}, pink marked areas), ν(C-H) (1150–1450 cm^{-1}, green marked areas), and δ(C-H), ν(C-N) (1030–1090 cm^{-1}). In addition, we can address the presence of some bands that are distinctive for the organic ligands such as ν(C-C) (729 cm^{-1}) for the NP(t-Bu)$_2$ (Figure S4b) and ν(in-plane aromatic C-H) (1000 cm^{-1}) for the NP(Ph)$_2$ (Figure S4a) [26,37,38].

3.2. FADH Catalysis

3.2.1. Evolution of Catalytic-Solution Potential (Eh)

Figure 1 presents the E_h profiles of the homogeneous [$NP(Ph)_2/Fe^{II}/PP_3$] and [$NP(t\text{-}Bu)_2/Fe^{II}/PP_3$] and the heterogeneous analogues [SiO_2@$NP(Ph)_2/Fe^{II}/PP_3$] and [SiO_2@$NP(t\text{-}Bu)_2/Fe^{II}/PP_3$] as recorded using a molar [Fe^{II}:NP:PP_3] ratio equal to [1:2:1] during the first hour of the catalytic operation. As is depicted in Figure 1, the E_h profiles exhibited clear stepwise trends that correspond to the reaction steps:

(i) Initially, a slight decrease in E_h occurred in all cases, as shown in Figure 1a–d where the addition of FA, Fe^{II}, and NP-ligands resulted in the profiles maintaining their positive values.

(ii) In all cases, the E_h profiles attained negative values, i.e., between −70 and −108 mV, when the poly-phosphine ligand, PP3, was introduced. This was followed by the production of gases (CO_2 + H_2, as confirmed by the GC-TCD analysis), which was visually evident by the vigorous formation of bubbles.

(iii) After 10 min of gas production (CO_2 + H_2), the E_h profile was shifted to more negative values and remained in this way for a period of 30–40 min, as shown in Figure 1a–d. As analyzed originally, for the case of the homogeneous Fe catalysts, these negative E_h values signify the formation of active Fe-hydride species [29] that are the key catalytic species. Thus, our data verifies that E_h profiles are a useful tool to monitor the catalytic evolution of the present homogenous and heterogeneous catalytic systems. Noticeably, in Figure 1b,c, an increase in the E_h profile was observed in the heterogeneous systems when approaching the end of the catalytic procedure.

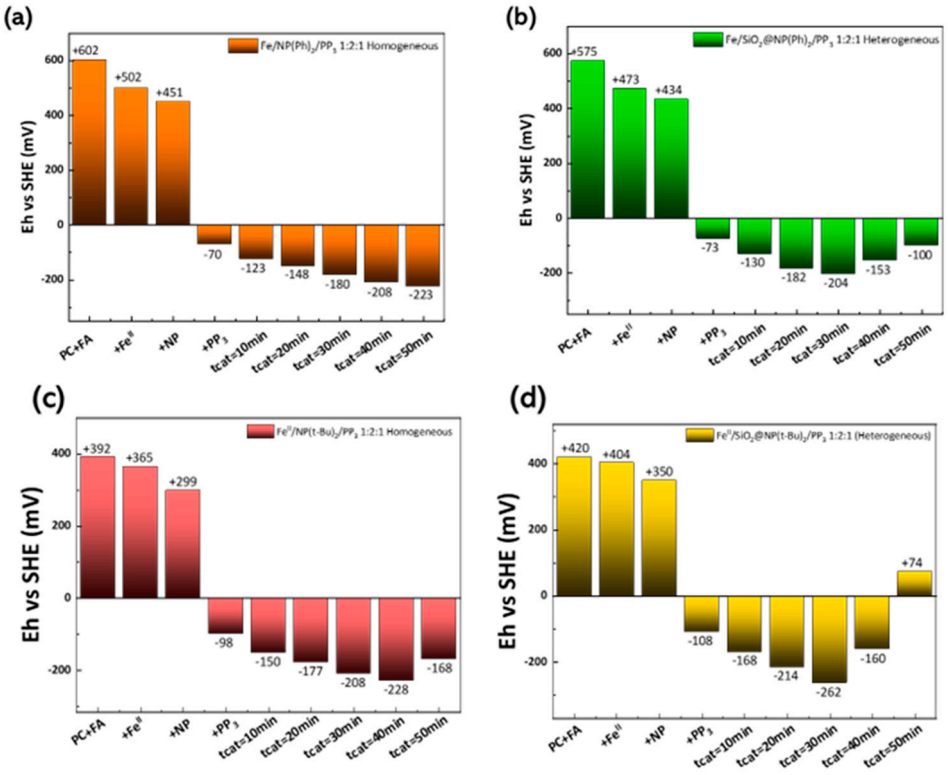


Figure 1. Solution potential profile (E_h vs. SHE) for homogeneous [$NP(Ph)_2/Fe^{II}/PP_3$] (orange) and [$NP(t\text{-}Bu)_2/Fe^{II}/PP_3$] (pink), as well as heterogeneous [SiO_2@$NP(Ph)_2/Fe^{II}/PP_3$] (green) and [SiO_2@$NP(t\text{-}Bu)_2$/ Fe^{II}/PP_3] (yellow) catalytic systems. Conditions: 5 mL of PC, 2 mL of FA, 7.5 μmol of $Fe(BF_4)_2{\cdot}6H_2O$, (**a**) 15 μmol of $NP(Ph)_2$, (**b**) 15 μmol of SiO_2@$NP(Ph)_2$ (50 mg), (**c**) 15 μmol of $NP(t\text{-}Bu)_2$, (**d**) 15 μmol of SiO_2@$NP(t\text{-}Bu)_2$ (75 mg), and 7.5 μmol PP_3 in 80 °C.

3.2.2. Kinetics of FADH

Figure 2 presents the kinetics of gas production from 2 mL of HCOOH, using the present catalysts until the time when there was no longer any formation of gas observed. The GC-TCD analysis shows that the gasses produced consist exclusively of H_2 and CO_2 in a [1:1] ratio, with no CO (Figure S5).

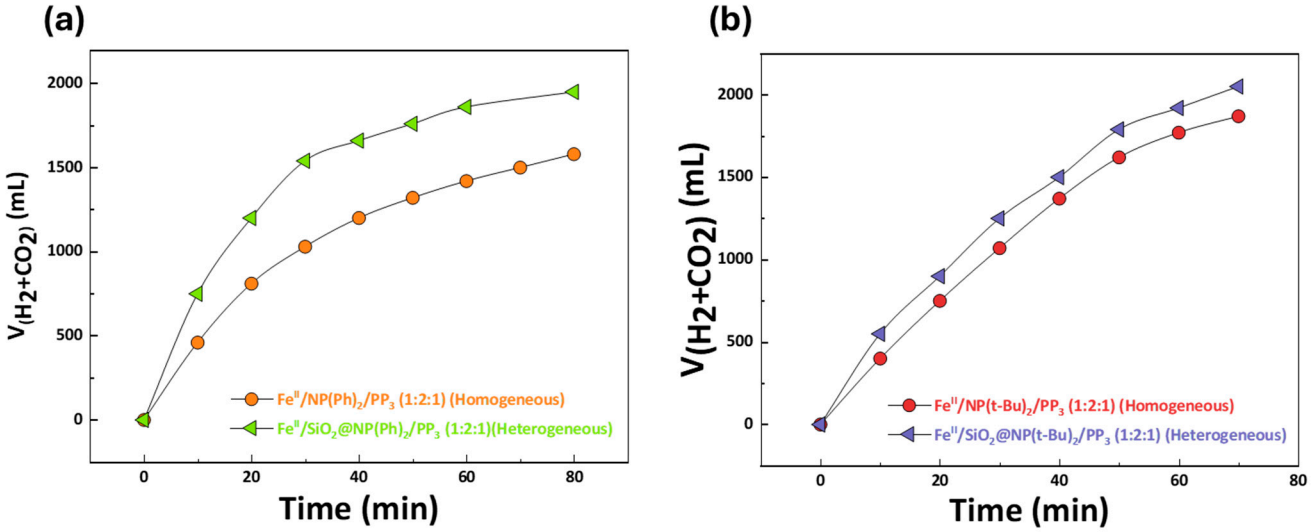


Figure 2. Volume of gasses (mL) (H_2 + CO_2) produced over time (min) from 2 mL of formic acid using (**a**) [NP(Ph)$_2$/Fe^{II}/PP$_3$] (orange) and [SiO$_2$@NP(Ph)$_2$/Fe^{II}/PP$_3$] (light green), as well as (**b**) [NP(t-Bu)$_2$/Fe^{II}/PP$_3$] (red) and [SiO$_2$@NP(t-Bu)$_2$/ Fe^{II}/PP$_3$] (light purple). Conditions: 5 mL of PC, 2 mL of FA, 7.5 μmol of Fe(BF$_4$)$_2$·6H$_2$O, (**a**) 15 μmol of NP(Ph)$_2$ or SiO$_2$@NP(Ph)$_2$, (**b**) 15 μmol of NP(t-Bu)$_2$ or SiO$_2$@NP(t-Bu)$_2$, and 7.5 μmol of PP$_3$ in 80 °C.

According to Figure 2, employing dehydrogenation of 2 mL of HCOOH, the homogeneous [NP(t-Bu)$_2$/Fe^{II}/PP$_3$] produced 1870 mL of gases over a 70 min operation, achieving a TONs = 5097 and a TOFs = 4356 h^{-1}, while the heterogeneous [SiO$_2$@NP(t-Bu)$_2$/Fe^{II}/PP$_3$] achieved a superior production rate, i.e., 2050 mL in the same time frame, with a TON of 5097 and a TOF of 4356 h^{-1}. The homogeneous [NP(Ph)$_2$/Fe^{II}/PP$_3$] system generated 1580 mL of [H_2 + CO_2] in 80 min with a TON = 4307 and a TOF = 3133 h^{-1}. As in the case of [NP(t-Bu)$_2$/Fe^{II}/PP$_3$], the immobilization of the NP(Ph)$_2$ ligand on the SiO$_2$ matrix improved the catalyst's efficiency, i.e., the heterogeneous [SiO$_2$@NP(Ph)$_2$/Fe^{II}/PP$_3$] system produced 1950 mL of gas within the same operating time, with a TONs of 5316 and a TOFs of 4089 h^{-1}. The findings from the Eh mapping and the kinetic dehydrogenation experiment correlate with this, as for the heterogeneous systems, both the gas production rate and volume significantly decrease after approximately 30 min of operation. Overall, the data in Figure 2 exemplify that [SiO$_2$@NP(t-Bu)$_2$/ Fe^{II}/PP$_3$] and [SiO$_2$@NP(Ph)$_2$/ Fe^{II}/PP$_3$] are heterogeneous catalysts that can outperform their parental homogeneous catalysts. This is a non-evident observation, as typically in all cases reported so far, including ours, the heterogeneous systems show slower FADH kinetics than their homogeneous counter parts. This implies that the present heterogeneous systems have certain thermodynamic advantages that render them able to overcome the inherent kinetic/diffusion limitations, a point that is studied and supported hereafter by an Arrhenius analysis.

3.2.3. Continuous Feeding of Formic Acid

Catalytic assessments under continuous operation were conducted, as employed in our previous works [26]. The procedure is as follows: 1 mL of FA was added every time that 1200 mL of gases were produced, (see Figure 3, where every point marked by an

arrow corresponds with the addition of 1 mL of FA). Note that 1200 mL (CO_2 + H_2) is equal to the catalytic products of 1 mL of FA. Additions of FA were repeated until gas generation stopped, or the systems' performance was significantly decreased, mainly due to the progressive accumulation of inhibiting factors such as H_2O from the commercial HCOOH used [26].

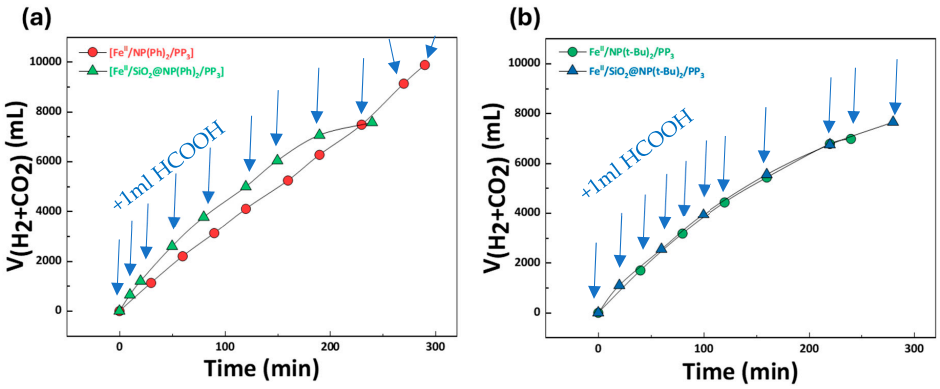


Figure 3. Continuous catalytic operation of systems: (**a**) [$NP(Ph)_2/Fe^{II}/PP_3$] (circular red line), [SiO_2@$NP(Ph)_2/Fe^{II}/PP_3$] (triangle light green line) and (**b**) [$NP(t\text{-}Bu)_2/Fe^{II}/PP_3$] (circular green line), [SiO_2@$NP(t\text{-}Bu)_2/Fe^{II}/PP_3$] (triangle blue line). Every arrow over a point indicates the addition of a new amount of FA (1 mL). Conditions: 5 mL of PC, 2 mL of FA, 7.5 µmol of $Fe(BF_4)_2{\cdot}6H_2O$, (**a**) 15 µmol of $NP(Ph)_2$ or SiO_2@$NP(Ph)_2$ (50 mg), (**b**) 15 µmol of $NP(t\text{-}Bu)_2$ or SiO_2@$NP(t\text{-}Bu)_2$ (75 mg), and 7.5 µmol of PP_3 in 80 °C.

The data in Figure 3 show that under this experimental set up, both the homogeneous [$NP(Ph)_2/Fe^{II}/PP_3$] (Figure 3a, red points) and heterogeneous [SiO_2@$NP(Ph)_2/Fe^{II}/PP_3$] (Figure 3a, light green points) systems successfully operated in FADH catalysis and produced 9880 mL and 7750 mL of [H_2 + CO_2], respectively. Regarding their TOFs, these systems achieved 5611 h^{-1} and 5159 h^{-1}, respectively (Table 1). The homogeneous catalyst [$NP(t\text{-}Bu)_2/Fe^{II}/PP_3$] (Figure 3b, green points) and the heterogeneous catalyst [SiO_2@$NP(t\text{-}Bu)_2/Fe^{II}/PP_3$] (Figure 3b, dark blue points) manage to produce 6980 mL and 7650 mL of gases, respectively (Table 1); in terms of their TOFs, these complexes achieved 4757 h^{-1} and 4465 h^{-1}, respectively.

Table 1. Catalytic results for [NP-based ligand/Fe^{II}/PP_3] systems for FADH, upon continuous addition of formic acid.

Catalytic System	V_{tot} (mL)	TONs	TOFs (h^{-1})	V_{FA} (mL)	Rate (mL/min)
Homogeneous					
[$NP(Ph)_2/Fe^{II}/PP_3$]	9880	26,933	5611	10	37.7
[$NP(t\text{-}Bu)_2/Fe^{II}/PP_3$]	6980	19,028	4757	6	42.5
Heterogeneous					
[SiO_2@$NP(Ph)_2/Fe^{II}/PP_3$]	7570	20,636	5159	8	58.0
[SiO_2@$NP(t\text{-}Bu)_2/Fe^{II}/PP_3$]	7650	20,854	4465	7	55.0

Recycling Experiments and Spectroscopy Analysis of the Recovered Materials

Recycling catalytic experiments were also conducted for the heterogeneous systems. For this, the materials were recovered by centrifugation (6000 rpm), washed with methanol, and dried under vacuum for 24 h at 40 °C. We underline that the recovered catalysts were used for FADH catalysis with no further addition of Fe^{II}. Under this experimental set-up, the reused catalytic systems provided approximately 1 L of gases, which is significantly decreased compared to their first cycle of use. To address this finding, following the FADH

catalysis, a spectroscopic analysis of the recovered materials was conducted using FT-IR and Raman spectroscopy with those spectra being compared to those of the pristine hybrid materials (Figures S6 and S7 in Supplementary Materials). The Raman and FT-IR spectroscopic changes revealed the decreased intensity or disappearance of certain bands, indicating possible degradation or leaching of the grafted ligands (Figures S6 and S7 in Supplementary Materials). More specifically, changes were detected in the bands referring to the aromatic and aliphatic C-H stretching vibrations, i.e., the disappearance of the band at 2928 cm^{-1} (Figure S6) as well as of the band at 2855 cm^{-1} (Figure S7) referring to the vibrations of the aliphatic C-H. At the same time, a shift to lower wavenumbers (from 592 cm^{-1} to 571 cm^{-1}) (Figure S6) indicates the coordination of Fe^{II} to the P-atom, affecting the vibrations of the P-C bond, and indicating the tracing of Fe^{II} incorporation into the hybrids during their use in FADH catalysis, possibly without it being enough for the catalyst to show any signs of higher recyclability. Furthermore, as shown in Figure S6, for the retrieved SiO_2@NP$(Ph)_2$ (green line), the formation of a new band at 1789 cm^{-1} appeared, corresponding to the stretching vibrations of the C=O bond of HCOOH, while a broadened peak at 1801 cm^{-1} developed (Figure S7), resembling the C-O and C=O stretching vibrations, respectively [28,39,40], in alignment with the perception of an interaction between the hybrids and formic acid during catalysis. Moreover, the signal at 962 cm^{-1} is a result of the vibrations from $HCOO^-$, which is probably adsorbed to the surface of SiO_2 [41].

3.3. Arrhenius Analysis

For a thermodynamic study on the [NP$(Ph)_2$/Fe^{II}/PP_3], [SiO_2@NP$(Ph)_2$/Fe^{II}/PP_3], [NP(t-Bu)$_2$/Fe^{II}/PP_3], and [SiO_2@NP(t-Bu)$_2$/Fe^{II}/PP_3] systems in FADH catalysis, the gas production over time, which is driven by every system, was measured at different temperatures (90, 85, 80, 70, and 60 °C), as presented in Figures 4 and 5. The calculated TOF values were applied to the Arrhenius equation [28,42]:

$$\ln TOF = -\frac{Ea}{R} \times \left(\frac{1}{T}\right) + c \quad (3)$$

where Ea is the activation energy of the system in J/mol, T is the temperature in K, and R = 8.314 J/K·mol. In this way, the Arrhenius plots were created. See Figure 4a,b for the [NP$(Ph)_2$/Fe^{II}/PP_3] and [SiO_2@NP$(Ph)_2$/Fe^{II}/PP_3] plots, where the insets show the corresponding gas production over time at the given temperatures. Based on the linear Arrhenius fitting using Equation (3), the homogeneous system [NP$(Ph)_2$/Fe^{II}/PP_3] was found to have an activation energy equal to Ea = 37.0 KJ/mol, while its heterogeneous counterpart [SiO_2@NP$(Ph)_2$/Fe^{II}/PP_3] had an Ea = 29.4 KJ/mol, as listed in Table 2. The significant decrease in activation energy of the heterogeneous system [NP$(Ph)_2$/Fe^{II}/PP_3] compared to the homogeneous system aligns with the higher catalytic activity of [SiO_2@NP$(Ph)_2$/Fe^{II}/PP_3].

Table 2. Activation energy and gas production rate for [Fe^{II}/PP_3] and [Fe^{II}/NP-based ligand/PP_3] systems in FADH catalysis.

Catalytic System	Ea (KJ/mol)	Gas Production Rate from FADH (mL/min)
[Fe^{II}/PP_3]	77.9	31.4
[NP(t-Bu)$_2$/Fe^{II}/PP_3]	54.0	42.5
[SiO_2@NP(t-Bu)$_2$/Fe^{II}/PP_3]	50.6	55.0
[NP$(Ph)_2$/Fe^{II}/PP_3]	37.0	37.7
[SiO_2@NP$(Ph)_2$/Fe^{II}/PP_3]	29.4	58.0

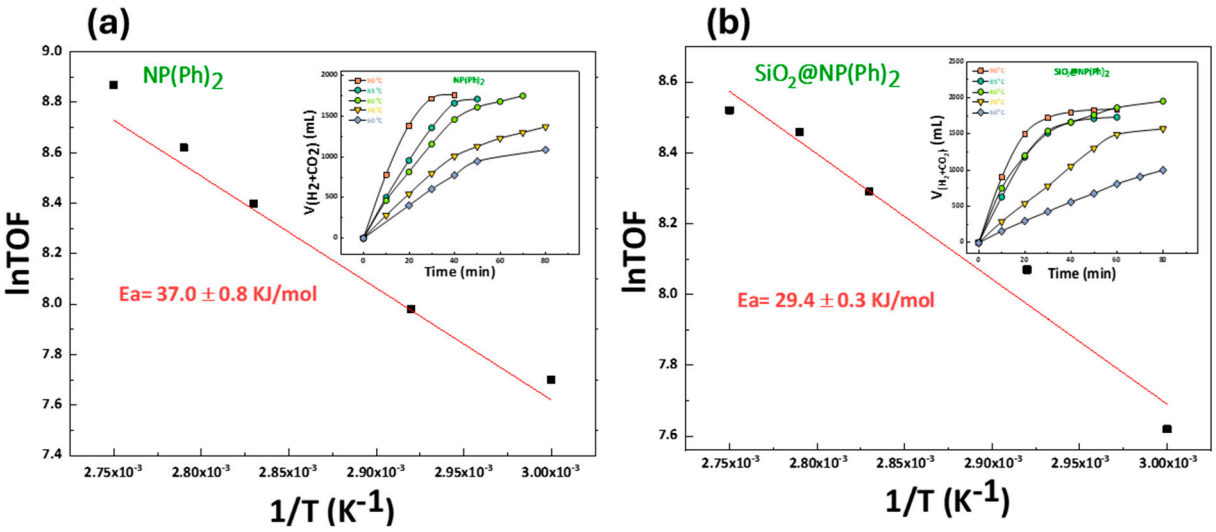


Figure 4. Linear Arrhenius plots for [$NP(Ph)_2/Fe^{II}/PP_3$] (**a**) and [SiO_2@$NP(Ph)_2/Fe^{II}/PP_3$] (**b**). Insets: Gas production over time at different temperatures by [$NP(Ph)_2/Fe^{II}/PP_3$] (**a**) and [SiO_2@$NP(Ph)_2/Fe^{II}/PP_3$] (**b**).

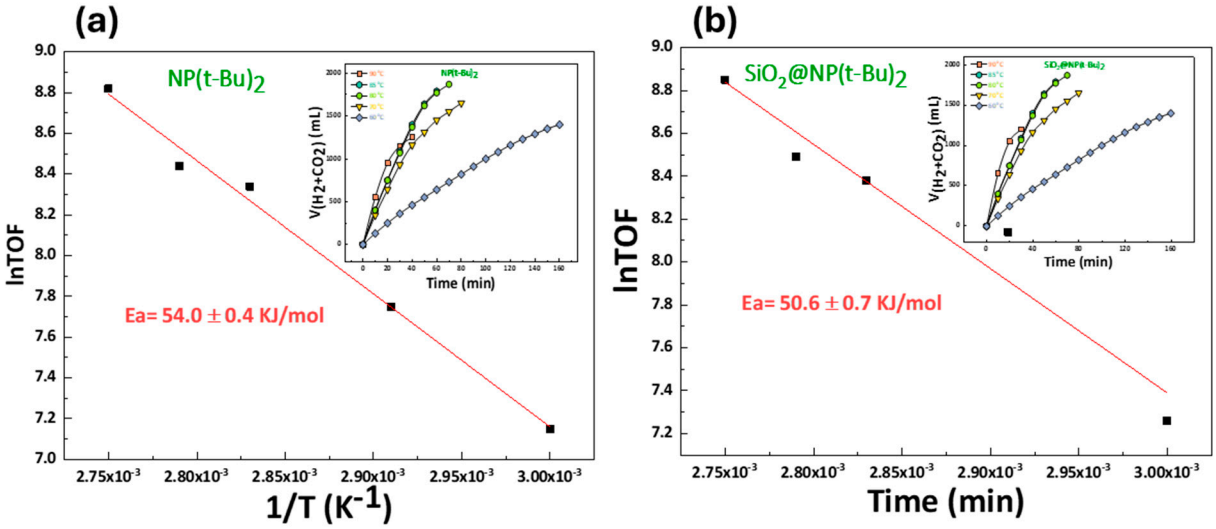


Figure 5. Linear Arrhenius plots for [$NP(t\text{-}Bu)_2/Fe^{II}/PP_3$] (**a**) and [$SiO_2$@$NP(t\text{-}Bu)_2/Fe^{II}/PP_3$] (**b**). Insets: Gas production over time at different temperatures by [$NP(t\text{-}Bu)_2/Fe^{II}/PP_3$] (**a**) and [$SiO_2$@$NP(t\text{-}Bu)_2/Fe^{II}/PP_3$] (**b**).

Figure 5 shows the Arrhenius plots for the [$NP(t\text{-}Bu)_2/Fe^{II}/PP_3$] and [$SiO_2$@$NP(t\text{-}Bu)_2/Fe^{II}/PP_3$] catalytic systems. The calculated activation energy for the homogeneous [$NP(t\text{-}Bu)_2/Fe^{II}/PP_3$] system was calculated to be at Ea = 54.0 KJ/mol and for the heterogeneous [SiO_2@$NP(t\text{-}Bu)_2/Fe^{II}/PP_3$], it decreased to Ea = 50.6 KJ/mol, as listed in Table 2. In an analogous way, the activation energy for [Fe^{II}/PP_3] was also calculated for comparison reasons (See Figure S8) and it was found to be 77.9 KJ/mol, which is very close to the literature value [20].

Based on the E_a values in Table 2, the positive impact of the "double-ligand" strategy is already evident from the reduction in activation energy values that was observed in the homogeneous systems involving [Fe^{II}/PP_3] and [Fe^{II}/NP-based ligands/PP_3], in the following order: Ea[Fe^{II}/PP_3] = 77.9 KJ/mol > Ea[$NP(t\text{-}Bu)_2/Fe^{II}/PP_3$] = 54.0 KJ/mol > Ea[$NP(Ph)_2/Fe^{II}/PP_3$] = 37.0 KJ/mol. In addition, the grafting of the NP ligands onto the surface of SiO_2 further decreases the activation energy as follows (Table 2): Ea[$NP(t\text{-}Bu)_2/Fe^{II}/PP_3$] = 54.0 KJ/mol > Ea[$SiO_2$@$NP(t\text{-}Bu)_2$/ Fe^{II}/PP_3] = 50.6 KJ/mol and

Ea[$NP(Ph)_2/Fe^{II}/PP_3$] = 37.0 KJ/mol > Ea[SiO_2@$NP(Ph)_2/Fe^{II}/PP_3$] = 29.4 KJ/mol, indicating that the ligands' immobilization has a further beneficial impact on FADH catalysis.

To understand these trends, Figure 6 demonstrates that an anti-correlation is occurring between the Ea values and the FADH gas production rates. As shown in Figure 6, a decrease in activation energy leads to an increase in the rate: the homogeneous [Fe^{II}/PP_3] system shows the highest Ea combined with the lowest rate of gas production. That is, the thermodynamic approach to developing efficient systems for FADH catalysis, parallel to the enhanced rates, provides additional evidence for the positive effect that the adoption of the "double-ligand" concept combined with the use of PN-type ligands has on catalytic H_2 production.

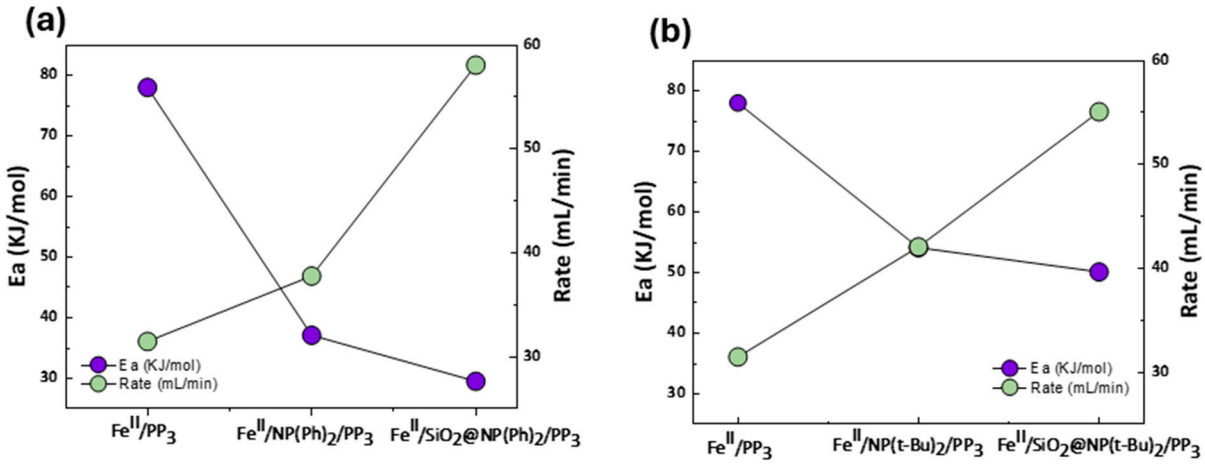


Figure 6. Ea (KJ/mol) vs. {[H_2 + CO_2] FADH gas production rate (mL/min)} for the catalytic systems (**a**) [Fe^{II}/PP_3], [$NP(t\text{-}Bu)_2/Fe^{II}/PP_3$], and [$SiO_2$@$NP(t\text{-}Bu)_2/Fe^{II}/PP_3$] and (**b**) [$Fe^{II}/PP_3$], [$NP(Ph)_2/Fe^{II}/PP_3$], and [$SiO_2$@$NP(Ph)_2/Fe^{II}/PP_3$].

4. Conclusions

Overall, the present data reveal that among the catalytic systems, the highest catalytic performance was exhibited by the heterogeneous [SiO_2@$NP(Ph)_2/Fe^{II}/PP_3$] system, producing 7570 mL of gas with continuous FA feeding, and achieving a total TON of 20,636 and a TOF of 5159 h^{-1}. This performance has a thermodynamic background as a decrease in activation energy by up to 21% for [Fe^{II}/SiO_2@$NP(Ph)_2/PP_3$] was demonstrated through an Arrhenius analysis. The observed decrease in the Ea of [SiO_2@NP-ligands/Fe^{II}/PP_3] vs. the homogeneous [NP-ligands/Fe^{II}/PP_3] is directly anti-correlated with higher rates of gas production in both case studies presented here.

We can consider that this thermodynamic/catalytic advantage seen with the heterogeneous systems may be due to the presence of a docking platform offered by the silica support, ultimately facilitating FADH catalysis. This effect was evidenced in our previous works as well [28]. Herein, the distinct cases of the heterogeneous [SiO_2@$NP(Ph)_2/Fe^{II}/PP_3$] and [SiO_2@$NP(t\text{-}Bu)_2/Fe^{II}/PP_3$] systems represent the first heterogeneous systems that outperform their homogeneous parental counterparts.

Overall, for the first time, the association between the activation energies of the developed systems and the rates of production was made apparent, leading to the conclusion that a lower activation energy clearly corresponds to a higher H_2 + CO_2 gas production rate via FADH, a result coming together with the enactment of the "double-ligand" strategy.

In a broader context, the present study exemplifies clearly that diligent engineering of materials allows for a credible realization of the envisioned low-cost, additive-free hydrogen production under mild conditions, offering solutions to hydrogen storage challenges. Lastly, our findings herein underline the effectiveness of the "double-ligand" approach

and the relationship between reduced activation energy and increased production rates, providing even more validation that this strategy is important for advancing cleaner energy technologies.

Supplementary Materials: The following supporting information can be downloaded at: https://www.mdpi.com/article/10.3390/en18030514/s1, Equation (S1): Calculation of TON values; Equation (S2): Calculation of TOF values; Figure S1: TG-DTA thermograph of SiO_2@NP(Ph)$_2$; Figure S2: TG-DTA thermograph of SiO_2@NP(t-Bu)$_2$; Figure S3: FT-IR spectra of (a) SiO_2@NP(Ph)$_2$ and (b) SiO_2@NP(t-Bu)$_2$; Figure S4: Raman spectra of (a)SiO_2@NP(Ph)$_2$ and (b) SiO_2@NP(t-Bu)$_2$; Figure S5: Gas Chromatography (GC) analysis of gas produced by [SiO_2@NP(t-Bu)$_2$/Fe^{II}/PP_3] system; Figure S6: FT-IR of SiO_2@NP(Ph)$_2$ after FADH; Figure S7: FT-IR of SiO_2@NP(t-Bu)$_2$ after FADH; Figure S8: Raman of SiO_2@NP(Ph)$_2$ after FADH; Figure S9: Raman of SiO_2@NP(t-Bu)$_2$ after FADH; Figure S10: Linear Arrhenius plot for [Fe^{II}/PP_3]. Inset: Gas production over time at different temperatures for [Fe^{II}/PP_3].

Author Contributions: Conceptualization, M.L. and Y.D.; Methodology, A.S. and E.A.; Formal analysis, A.S., M.L. and Y.D.; Investigation, A.S. and E.A.; Data curation, A.S. and E.A.; writing—original draft preparation, A.S.; writing—review and editing, A.S., Y.D. and M.L.; Supervision, M.L. and Y.D. All authors have read and agreed to the published version of the manuscript.

Funding: This research received no external funding.

Data Availability Statement: The original contributions presented in this study are included in the article/Supplementary Materials, and further inquiries can be directed to the corresponding author.

Conflicts of Interest: The authors declare no conflicts of interest.

References

1. Solakidou, M.; Theodorakopoulos, M.; Deligiannakis, Y.; Louloudi, M. Double-Ligand Fe, Ru Catalysts: A Novel Route for Enhanced H_2 Production from Formic Acid. *Int. J. Hydrog. Energy* **2020**, *45*, 17367–17377. [CrossRef]
2. Mazloomi, K.; Gomes, C. Hydrogen as an Energy Carrier: Prospects and Challenges. *Renew. Sustain. Energy Rev.* **2012**, *16*, 3024–3033. [CrossRef]
3. Navlani-García, M.; Martis, M.; Lozano-Castelló, D.; Cazorla-Amorós, D.; Mori, K.; Yamashita, H. Investigation of Pd Nanoparticles Supported on Zeolites for Hydrogen Production from Formic Acid Dehydrogenation. *Catal. Sci. Technol.* **2015**, *5*, 364–371. [CrossRef]
4. Dincer, I. Renewable Energy and Sustainable Development: A Crucial Review. *Renew. Sustain. Energy Rev.* **2000**, *4*, 157–175. [CrossRef]
5. Nguyen, K.H.; Kakinaka, M. Renewable Energy Consumption, Carbon Emissions, and Development Stages: Some Evidence from Panel Cointegration Analysis. *Renew. Energy* **2019**, *132*, 1049–1057. [CrossRef]
6. Bulushev, D.A.; Ross, J.R.H. Towards Sustainable Production of Formic Acid. *ChemSusChem* **2018**, *11*, 821–836. [CrossRef]
7. Mellmann, D.; Sponholz, P.; Junge, H.; Beller, M. Formic Acid as a Hydrogen Storage Material–Development of Homogeneous Catalysts for Selective Hydrogen Release. *Chem. Soc. Rev.* **2016**, *45*, 3954–3988. [CrossRef] [PubMed]
8. Coffey, R.S. The Decomposition of Formic Acid Catalysed by Soluble Metal Complexes. *Chem. Commun.* **1967**, 923b. [CrossRef]
9. Gao, Y.; Kuncheria, J.; Puddephatt, R.J.; Yap, G.P.A. An Efficient Binuclear Catalyst for Decomposition of Formic Acid. *Chem. Commun.* **1998**, 2365–2366. [CrossRef]
10. Fellay, C.; Dyson, P.J.; Laurenczy, G. A Viable Hydrogen-Storage System Based On Selective Formic Acid Decomposition with a Ruthenium Catalyst. *Angew. Chem. Int. Ed.* **2008**, *47*, 3966–3968. [CrossRef]
11. Himeda, Y. Highly Efficient Hydrogen Evolution by Decomposition of Formic Acid Using an Iridium Catalyst with 4,4′-Dihydroxy-2,2′-Bipyridine. *Green Chem.* **2009**, *11*, 2018. [CrossRef]
12. Loges, B.; Boddien, A.; Junge, H.; Beller, M. Controlled Generation of Hydrogen from Formic Acid Amine Adducts at Room Temperature and Application in H_2 /O_2 Fuel Cells. *Angew. Chem. Int. Ed.* **2008**, *47*, 3962–3965. [CrossRef] [PubMed]
13. Boddien, A.; Loges, B.; Junge, H.; Beller, M. Hydrogen Generation at Ambient Conditions: Application in Fuel Cells. *ChemSusChem* **2008**, *1*, 751–758. [CrossRef]
14. Solakidou, M.; Gemenetzi, A.; Koutsikou, G.; Theodorakopoulos, M.; Deligiannakis, Y.; Louloudi, M. Cost Efficiency Analysis of H_2 Production from Formic Acid by Molecular Catalysts. *Energies* **2023**, *16*, 1723. [CrossRef]

15. Pan, Y.; Pan, C.; Zhang, Y.; Li, H.; Min, S.; Guo, X.; Zheng, B.; Chen, H.; Anders, A.; Lai, Z.; et al. Selective Hydrogen Generation from Formic Acid with Well-Defined Complexes of Ruthenium and Phosphorus–Nitrogen PN^3 -Pincer Ligand. *Chem. Asian J.* **2016**, *11*, 1357–1360. [CrossRef]
16. Onishi, N.; Kanega, R.; Kawanami, H.; Himeda, Y. Recent Progress in Homogeneous Catalytic Dehydrogenation of Formic Acid. *Molecules* **2022**, *27*, 455. [CrossRef]
17. Scotti, N.; Psaro, R.; Ravasio, N.; Zaccheria, F. A New Cu-Based System for Formic Acid Dehydrogenation. *RSC Adv.* **2014**, *4*, 61514–61517. [CrossRef]
18. Lu, Q.; Yu, H.; Fu, Y. Computational Study of Formic Acid Dehydrogenation Catalyzed by Al^{III} –Bis(Imino)Pyridine. *Chem. A Eur. J* **2016**, *22*, 4584–4591. [CrossRef]
19. Myers, T.W.; Berben, L.A. Aluminium–Ligand Cooperation Promotes Selective Dehydrogenation of Formic Acid to H_2 and CO_2. *Chem. Sci.* **2014**, *5*, 2771–2777. [CrossRef]
20. Boddien, A.; Mellmann, D.; Gärtner, F.; Jackstell, R.; Junge, H.; Dyson, P.J.; Laurenczy, G.; Ludwig, R.; Beller, M. Efficient Dehydrogenation of Formic Acid Using an Iron Catalyst. *Science* **2011**, *333*, 1733–1736. [CrossRef]
21. Zell, T.; Butschke, B.; Ben-David, Y.; Milstein, D. Efficient Hydrogen Liberation from Formic Acid Catalyzed by a Well-Defined Iron Pincer Complex under Mild Conditions. *Chem. A Eur. J* **2013**, *19*, 8068–8072. [CrossRef] [PubMed]
22. Curley, J.B.; Bernskoetter, W.H.; Hazari, N. Additive-Free Formic Acid Dehydrogenation Using a Pincer-Supported Iron Catalyst. *ChemCatChem* **2020**, *12*, 1934–1938. [CrossRef]
23. Anderson, N.H.; Boncella, J.; Tondreau, A.M. Manganese-Mediated Formic Acid Dehydrogenation. *Chem. A Eur. J.* **2019**, *25*, 10557–10560. [CrossRef]
24. Zhao, Y.; Deng, L.; Tang, S.-Y.; Lai, D.-M.; Liao, B.; Fu, Y.; Guo, Q.-X. Selective Decomposition of Formic Acid over Immobilized Catalysts. *Energy Fuels* **2011**, *25*, 3693–3697. [CrossRef]
25. Stathi, P.; Deligiannakis, Y.; Avgouropoulos, G.; Louloudi, M. Efficient H_2 Production from Formic Acid by a Supported Iron Catalyst on Silica. *Appl. Catal. A Gen.* **2015**, *498*, 176–184. [CrossRef]
26. Gkatziouras, C.; Solakidou, M.; Louloudi, M. Efficient [Fe-Imidazole@SiO_2] Nanohybrids for Catalytic H_2 Production from Formic Acid. *Nanomaterials* **2023**, *13*, 1670. [CrossRef]
27. Gkatziouras, C.; Solakidou, M.; Louloudi, M. Formic Acid Dehydrogenation over a Recyclable and Self-Reconstructing Fe/Activated Carbon Catalyst. *Energy Fuels* **2024**, *38*, 17914–17926. [CrossRef]
28. Theodorakopoulos, M.; Solakidou, M.; Deligiannakis, Y.; Louloudi, M. Double-Ligand [Fe/PNP/PP_3] and Their Hybrids [Fe/SiO_2@PNP/PP_3] as Catalysts for H_2-Production from HCOOH. *Energies* **2024**, *17*, 3934. [CrossRef]
29. Theodorakopoulos, M.; Deligiannakis, Y.; Louloudi, M. Solution-Potential and Solution-Hydrides as Key-Parameters in H_2 Production via HCOOH-Dehydrogenation by Fe- and Ru-Molecular Catalysts. *Int. J. Hydrog. Energy* **2024**, *58*, 1608–1617. [CrossRef]
30. Solakidou, M.; Deligiannakis, Y.; Louloudi, M. Heterogeneous Amino-Functionalized Particles Boost Hydrogen Production from Formic Acid by a Ruthenium Complex. *Int. J. Hydrog. Energy* **2018**, *43*, 21386–21397. [CrossRef]
31. Stathi, P.; Deligiannakis, Y.; Louloudi, M. Co-Catalytic Enhancement of H_2 Production by SiO_2 Nanoparticles. *Catal. Today* **2015**, *242*, 146–152. [CrossRef]
32. Capeletti, L.B.; Baibich, I.M.; Butler, I.S.; Dos Santos, J.H.Z. Infrared and Raman Spectroscopic Characterization of Some Organic Substituted Hybrid Silicas. *Spectrochim. Acta Part A Mol. Biomol. Spectrosc.* **2014**, *133*, 619–625. [CrossRef] [PubMed]
33. Fusè, M.; Rimoldi, I.; Cesarotti, E.; Rampino, S.; Barone, V. On the Relation between Carbonyl Stretching Frequencies and the Donor Power of Chelating Diphosphines in Nickel Dicarbonyl Complexes. *Phys. Chem. Chem. Phys.* **2017**, *19*, 9028–9038. [CrossRef]
34. Fragou, F.; Stathi, P.; Deligiannakis, Y.; Louloudi, M. Safe-by-Design Flame Spray Pyrolysis of SiO_2 Nanostructures for Minimizing Acute Toxicity. *ACS Appl. Nano Mater.* **2022**, *5*, 8184–8195. [CrossRef]
35. Kalampounias, A.G. IR and Raman Spectroscopic Studies of Sol–Gel Derived Alkaline-Earth Silicate Glasses. *Bull. Mater. Sci.* **2011**, *34*, 299–303. [CrossRef]
36. Ben Khemis, S.; Burov, E.; Montigaud, H.; Skrelic, D.; Gouillart, E.; Cormier, L. Structural Analysis of Sputtered Amorphous Silica Thin Films: A Raman Spectroscopy Investigation. *Thin Solid Film.* **2021**, *733*, 138811. [CrossRef]
37. Craig, P.J. Vibrational Spectra of Phosphorus Ligand Derivatives of Some Alkyltricarbonyl-π-Cyclopentadienylmolybdenum Compounds. *Can. J. Chem.* **1970**, *48*, 3089–3094. [CrossRef]
38. Saleem, M.; Majeed, M.I.; Nawaz, H.; Iqbal, M.A.; Hassan, A.; Rashid, N.; Tahir, M.; Raza, A.; Ul Hassan, H.M.; Sabir, A.; et al. Surface-Enhanced Raman Spectroscopy for the Characterization of the Antibacterial Properties of Imidazole Derivatives against *Bacillus Subtilis* with Principal Component Analysis and Partial Least Squares–Discriminant Analysis. *Anal. Lett.* **2022**, *55*, 2132–2146. [CrossRef]
39. Li, G.; Ridd, M.; Larkins, F. An Infrared Study of Formic Acid Adsorption on Co/SiO_2 and SiO_2 Surfaces. *Aust. J. Chem.* **1991**, *44*, 623. [CrossRef]

40. Theodorakopoulos, M.; Solakidou, M.; Deligiannakis, Y.; Louloudi, M. A Use-Store-Reuse (USR) Concept in Catalytic HCOOH Dehydrogenation: Case-Study of a Ru-Based Catalytic System for Long-Term USR under Ambient O_2. *Energies* **2021**, *14*, 481. [CrossRef]
41. Moussa, Z.; Judeh, Z.M.A.; Ahmed, S.A. Polymer-Supported Triphenylphosphine: Application in Organic Synthesis and Organometallic Reactions. *RSC Adv.* **2019**, *9*, 35217–35272. [CrossRef]
42. Peleg, M.; Normand, M.D.; Corradini, M.G. The Arrhenius Equation Revisited. *Crit. Rev. Food Sci. Nutr.* **2012**, *52*, 830–851. [CrossRef] [PubMed]

Disclaimer/Publisher's Note: The statements, opinions and data contained in all publications are solely those of the individual author(s) and contributor(s) and not of MDPI and/or the editor(s). MDPI and/or the editor(s) disclaim responsibility for any injury to people or property resulting from any ideas, methods, instructions or products referred to in the content.